



Probing dimensional consistency during multi-track multi-layer gas metal arc directed energy deposition of aluminium alloys

P. K. Chaurasia¹ · B. K. Barik¹ · A. Das² · S.-F. Goecke³ · A. De¹

Received: 16 August 2023 / Accepted: 10 January 2024 / Published online: 17 January 2024
© International Institute of Welding 2024

Abstract

The dimensional consistency of multi-track multi-layer parts fabricated by gas metal arc-directed energy deposition is by far the most critical challenge. A systematic investigation is presented here to examine the influence of the important process variables such as wire feed rate, printing travel speed and resulting energy input per unit length on the dimensional consistency and surface waviness of multi-track and multi-layer parts made by gas metal arc directed energy deposition using an aluminium alloy filler wire. The current and voltage transients are monitored in real-time to realize a quantitative measure of the arc power and energy input per unit length of deposition on the build profile and its dimensional consistency. The dimensional consistency and the surface waviness of the build profile are measured by optical microscopy. The microhardness distribution of the sample builds along the tracks and layers is also examined for different process conditions and the effect of energy input per unit length on microhardness distribution has been examined. The evaluation of the experimentally measured results shows that the dimensional inconsistency and surface unevenness of the deposited profiles can be reduced significantly by increasing the energy input per unit length for gas metal arc-directed energy deposition.

Keywords Additive manufacturing · Gas metal arc directed energy deposition · Aluminium alloy · Real-time monitoring · Dimensional consistency · Surface waviness · Microhardness

Abbreviations

GMAW	Gas metal arc welding
GMA-DED	Gas metal arc directed energy deposition
GTA-DED	Gas tungsten arc directed energy deposition
PTS	Printing travel speed/mm/s
WFR	Wire feed rate/m/min

List of variables

E	Energy input per unit length/J/mm
h	Track height/mm
h_e	Effective height/mm
h_t	Measured height/mm

I_a	Arc current/A
I_i	Instantaneous arc current/A
p	Penetration/mm
P	Arc power/W
t	Total cycle time/ms
t_B	Pulse-off time/ms
t_P	Pulse-on time/ms
t_i	Instantaneous time/ms
V_a	Arc voltage/V
V_i	Instantaneous arc voltage/V
w	Track width/mm
w_e	Effective width/mm
w_m	Measured width/mm
δ	Hatch spacing/mm

Recommended for publication by Commission XII - Arc Welding Processes and Production Systems

✉ P. K. Chaurasia
prashant9161@gmail.com

- ¹ Mechanical Engineering Department, Indian Institute of Technology Bombay, Mumbai 400076, India
- ² Materials Engineering Division, CSIR-National Metallurgical Laboratory, Jamshedpur 831007, India
- ³ Mechanical Engineering Department, University of Applied Sciences, 14770 Brandenburg an der Havel, Germany

1 Introduction

Gas metal arc directed energy deposition (GMA-DED) involves the melting and deposition of a continuously fed filler wire along multiple tracks and layers to quickly fabricate a three-dimensional part [1, 2]. GMA-DED is recognized for a high deposition rate and little material wastage, but the dimensional inconsistency and surface

waviness of the fabricated part are major challenges, which demand an appropriate selection of energy input and scanning strategy [2–5]. The real-time monitoring of current and voltage transients is the sole route for a true estimate of the actual arc power and energy input per unit length for different values of wire feed rate (WFR) and printing travel speed (PTS) in GMA-DED [6–8]. Detailed experimental investigations to realize the effect of important process conditions such as WFR, PTS, scanning strategy and hatch spacing on the dimensional consistency of the fabricated parts are currently evolving for GMA-DED [9, 10].

The dimensional inconsistency of the deposited tracks and layers is primarily attributed to improper process conditions [4, 11, 12], scanning strategy [13, 14] and the distortion of the part due to heat accumulation [15, 16]. Experimental investigations are conducted to identify the suitable process conditions [11], scanning strategies [13] and interpass temperature [17] to mitigate the dimensional inconsistency of the deposited part in GMA-DED of different alloys. Rodrigues et al. [12] reported that the dimensional uniformity of the deposited profiles improved with increasing energy input that was attributed to better wettability between the consecutive layers at higher energy input for single-track multi-layer GMA-DED with a steel filler wire. In contrast, Le et al. [18] found a reduced surface waviness at a lower energy input for single-track multi-layer GMA-DED with a 308L stainless steel filler wire. The bidirectional scanning strategy was found to be able to repair the craters and humps and improve the dimensional consistency of deposited tracks in comparison to unidirectional scanning [13, 14, 19, 20]. For gas tungsten arc directed energy deposition (GTA-DED) of aluminium alloy, Geng et al. [21] reported an increase in the surface waviness of single-track multi-layer walls at higher PTS and resulting reduced energy input per unit length of deposition. Overall, the influence of the energy input on the dimensional consistency of single-track and multi-track multi-layer GMA-DED of aluminium alloys is scarcely reported in literature. A suitable methodology for a quantitative assessment of surface waviness for single-track and multi-track multi-layer GMA-DED deposits is also in ever demand.

The distance between two overlapped tracks is referred to as hatch spacing and is an important process variable for GMA-DED that significantly influences the melt pool asymmetry [10, 22–24] and dimensional consistency of multi-track deposits [25, 26]. A suitable hatch spacing is required for a given process condition to reduce inconsistent track height, surface unevenness and lack-of-fusion defects [9, 27, 28]. Analytical models are reported in literature for a prior estimation of the hatch spacing [10, 29, 30], and a typical hatch spacing of around 72 to 76% of the width of a deposited track for a given process condition is found to provide a consistent deposit profile [9, 10, 29]. Further experimental

investigations to realize the sensitivity of dimensional consistency of multi-track multi-layer deposits to hatch spacing are of ever interest for GMA-DED.

In the present work, a systematic experimental investigation is carried out to investigate the influence of WFR, PTS and the resulting energy input on dimensional consistency, surface waviness and hardness of single-track and multi-track multi-layer GMA-DED using an aluminium filler wire. A real-time synchronous monitoring of current and voltage transients is undertaken to estimate the true arc power and the energy input. The transverse cross-sections of the sample deposits at multiple lengths are characterized for a quantitative estimation of dimensional consistency and microhardness distribution along the deposited tracks and layers.

2 Materials and methods

Figure 1a shows the experimental set-up with a worktable that is moveable along the X-Y plane and a GMA torch that can be moved along the Z-direction for the single-track multi-layer and multi-track multi-layer GMA-DED. The GMA torch can be set inclined in the direction as well as transverse to the direction of the travel during deposition. The PTS of the sliding worktable along the X-direction is controlled by a variable speed reversible servomotor. The hatch spacing for multi-track deposition is set by the transverse motion of the sliding worktable in the Y-direction using a calibrated knob. Likewise, the layer height for multi-layer deposition is set by the vertical movement of the GMA torch in the Z-direction using a calibrated knob.

Figure 1b shows the schematic for single-track GMA-DED with the GMA torch inclined at 75° along the deposition direction. A microprocessor-controlled, inverter-type, water-cooled GMAW power source (Alpha Q551 by EWM GmbH, Germany) is used with a wire feeder unit (Alpha Q drive 4L) and a liquid-cooled torch (KF 23E, KF 37E) for the deposition. The real-time current is monitored using a Hall effect closed loop current transducer (LEM LT 1005-S) along with an amplifier. The real-time voltage is monitored using an oscilloscope probe (PMT 212) connected between the contact tip of the torch and the substrate. The current and voltage transients are recorded using a pc-interfaced data acquisition system (Graphtec GL 900-4-UM-851) at a sampling rate of 100 kHz.

The sample deposits are prepared using a 1.0 mm diameter aluminium filler wire (AA4043) on an aluminium substrate (AA6061) of size 140 mm (length) × 80 mm (width) × 4 mm (thickness) as shown in Fig. 1b. The chemical composition (wt.%) of the filler wire and the substrate is presented in Table 1. Figure 1c shows the single-track multi-layer deposition with the bidirectional scanning strategy in which the start and the end positions are interchanged for the

printing of alternate layers [13, 20]. A bidirectional scanning strategy is used in the present work for the depositions of multiple parallel tracks as shown schematically in Fig. 1d with a suitable hatch spacing (δ). The hatch spacing (δ) for a given process conditions is estimated as $0.63 w$ where w is the width of the first deposited track [10]. Table 2 shows the three different combinations of WFR and PTS, which

are selected based on extensive trial experiments. These combinations are found to provide a consistent bead appearance and good wetting between the deposited tracks. The methodology for the estimation of other values in Table 2 is presented in Section 3.1.

A set of single-track five-layer and single-track nine-layer walls and five-track nine-layer builds are prepared

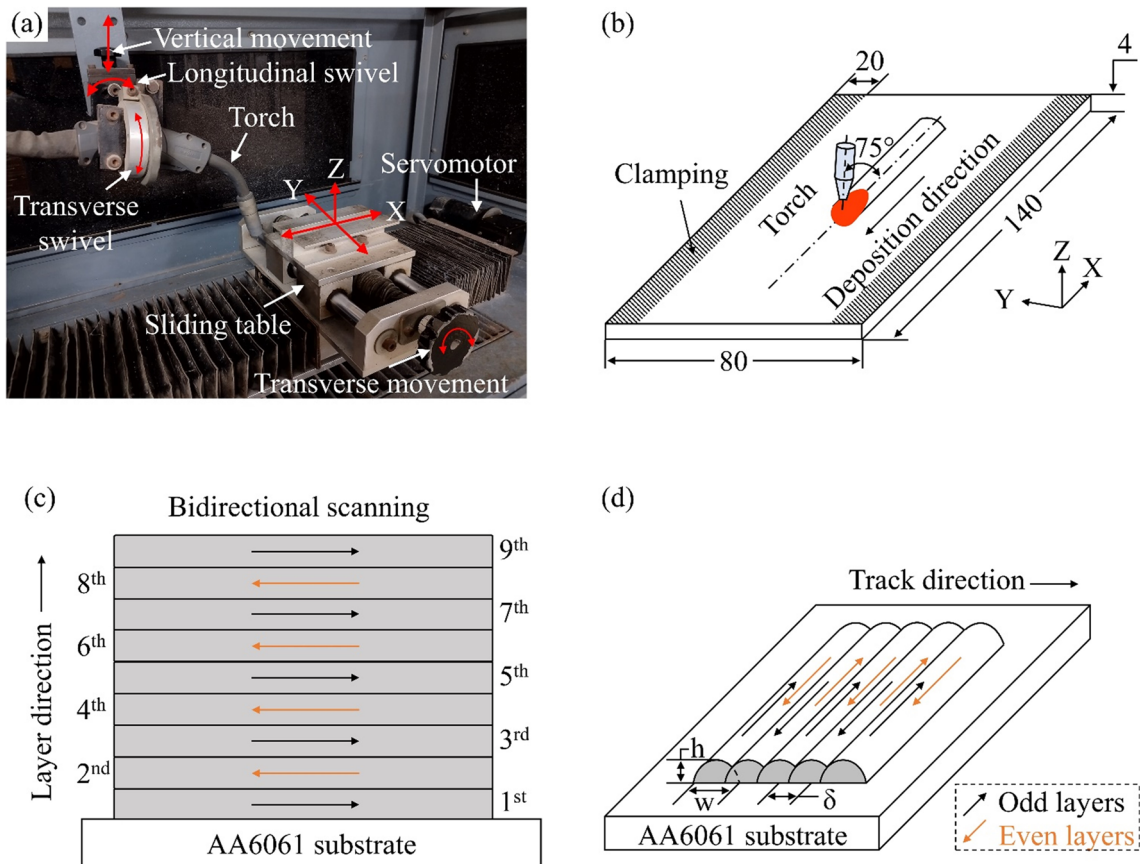


Fig. 1 **a** GMA-DED set-up including the deposition torch and worktable with the translational motion system (X-Y plane) and illustrations of **b** single-track deposition, **c** single-track nine-layer deposi-

tion with bidirectional scanning strategy and **d** five-track single-layer deposition with bidirectional tracks and layers. h , w and δ are track height, track width and hatch spacing, respectively

Table 1 Chemical composition (in wt.%) of substrate and filler wire

	Al	Mg	Fe	Si	Ti	Mn	Cu	Zn	Cr	UTS, MPa
Substrate (AA6061)	Bal.	1.01	0.59	0.59	0.02	0.14	0.24	0.16	0.12	322
Filler wire (AA4043)	Bal.	0.05	0.80	5.00	0.20	0.05	0.30	0.10	-	200

Table 2 Process conditions used for the deposition with the corresponding set numbers

Set no.	WFR	PTS	Time-averaged arc current	Time-averaged arc voltage	Time-averaged arc power	Energy input
	m/min	mm/s	I_a, A	V_a, V	P, W	$E, J/mm$
S1	5	5	42 (± 1)	18 (± 1)	818 (± 3)	163
S2	5	7.5	42 (± 1)	18 (± 1)	818 (± 3)	109
S3	6	7.5	61 (± 2)	21 (± 1)	1298 (± 5)	173

to examine the effect of process conditions on the dimensional consistency of the deposits. Two different numbers of layers (five and nine) are selected to examine the consistency of the results as a function of wall height. The deposits are always made in the middle of the substrate to provide a uniform rate of heat transfer from all sides through the substrate. The track length and the contact tip-to-work distance (CTWD) are kept fixed at 100 mm and 15 mm, respectively. Pure argon (99.999%) is used at a flow rate of 15 L/min as the shielding gas. A dwell time of around 1 min is used between the deposition of adjacent tracks and successive layers. The substrate plate is degreased and cleaned by acetone prior to the deposition and clamped along its edges as shown in Fig. 1b. Five samples are prepared for each condition and from each sample, three transverse sections near the mid-length of the deposit are polished and examined for detailed dimensional measurements. An average of all the measurements is considered for each condition. The samples are polished with emery paper and 0.25 μm diamond paste first. Further, the polished samples are etched with Keller's reagent and viewed under an optical microscope (Leica DM2500M) for dimensional measurements. The microhardness distribution through the deposits is measured at 1 mm equidistant locations using a Vickers microhardness tester (Model:

NVH-AUTO, Make: OMNI-TECH) with the load and dwell time of HV0.1 and 10 s, respectively.

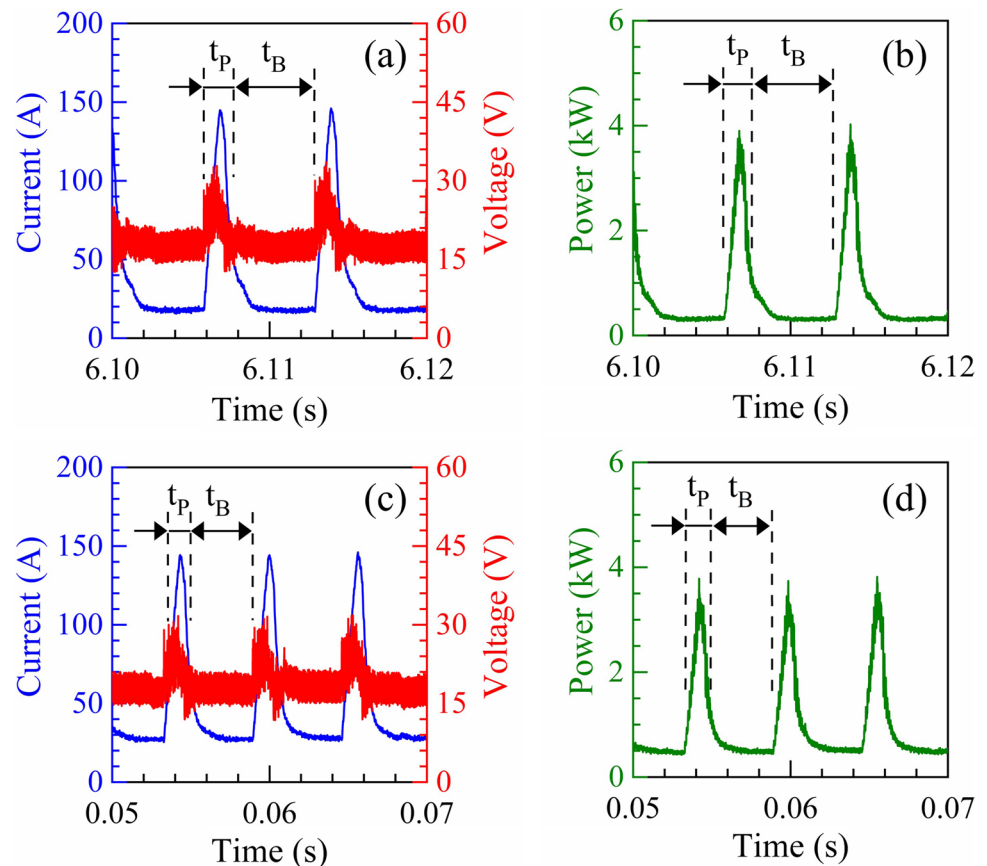
3 Results and discussion

3.1 Monitoring arc current, voltage and power

Figure 2 shows the current, voltage and arc power transients for two values of WFR for a small duration to depict the pulse-on and pulse-off phases. The current rises rapidly during the pulse-on time (t_p) to 143 (± 2) A and reduces to 18 (± 1) A in the pulse-off time (t_B) as shown in Fig. 2a for a WFR of 5 m/min. The corresponding arc power transient in Fig. 2b also shows a rapid rise during the pulse-on time (t_p) and a quick drop during the pulse-off time (t_B). The pulse-on (t_p) and pulse-off (t_B) times in Fig. 2a, b are 1.36 (± 0.40) ms and 5.30 (± 0.38) ms, respectively, and the pulse frequency is around 150 Hz. The peak current during the pulse-on period results in the rapid melting of the filler wire and the deposition of molten metal from the filler wire. A quick drop of the peak current in the pulse-off period reduces the overall arc power.

The time-averaged arc current (I_a), voltage (V_a) and power (P) are calculated using the following equations:

Fig. 2 Measured (a, c) current and voltage and (b, d) arc power transients for two WFRs of (a, b) 5 m/min and (c, d) 6 m/min. t_p and t_B are pulse-on and pulse-off time durations, respectively



$$I_a = \frac{\sum_{i=0}^t (I_i t_i)}{\sum_{i=0}^t (t_i)} \tag{1}$$

$$V_a = \frac{\sum_{i=0}^t (V_i t_i)}{\sum_{i=0}^t (t_i)} \tag{2}$$

$$P = \frac{\sum_{i=0}^t (V_i I_i t_i)}{\sum_{i=0}^t (t_i)} \tag{3}$$

where I_i , V_i and t_i refer to the instantaneous current, voltage and the time, respectively, at the i th time instant, and t is the summation of pulse-on and pulse-off times for a current pulse. For process conditions, the time-averaged arc current (I_a), voltage (V_a) and power (P) values are calculated for around fifty current pulses to compute their average values and the corresponding deviations. Table 2 presents the time-averaged arc current (I_a), voltage (V_a) and power (P) and the corresponding deviations for the three process conditions. Table 2 also depicts the energy input per unit length

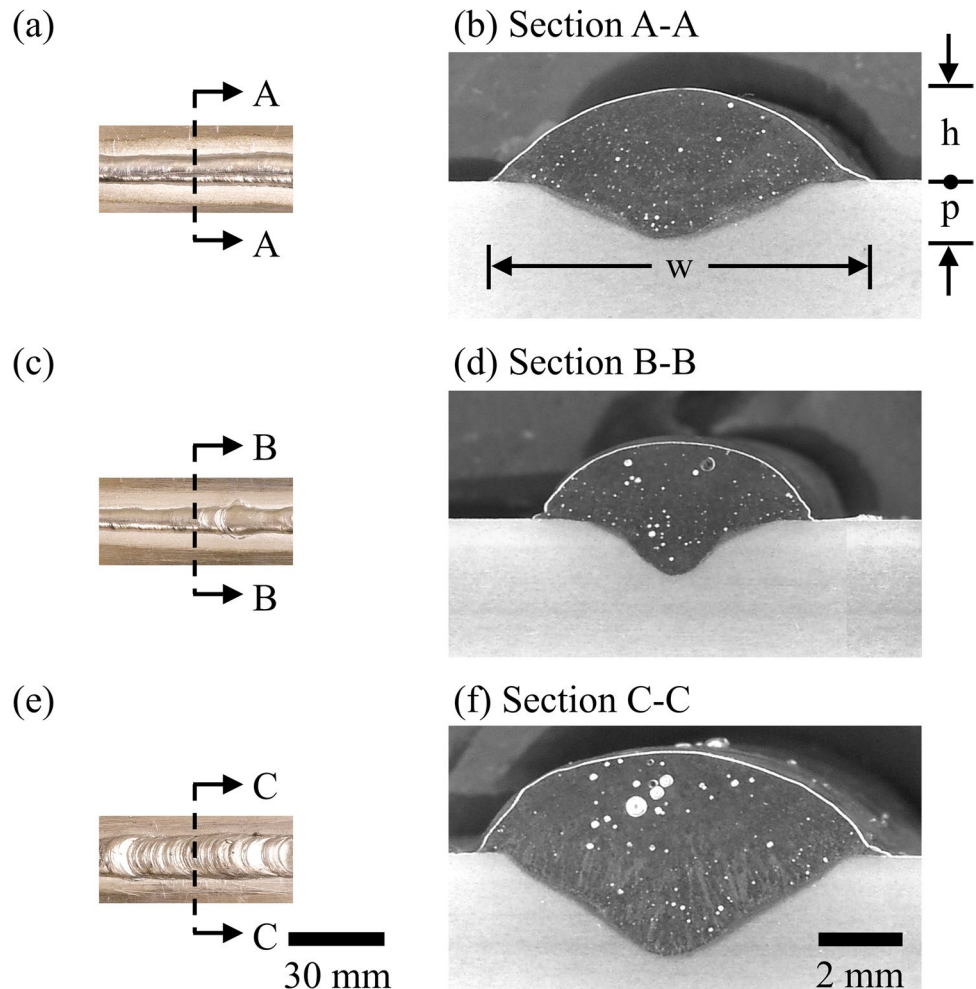
(E), which is estimated as a ratio of the time-averaged arc power (P) and the printing travel speed (PTS) for each process condition.

With an increase of the WFR from 5 to 6 m/min, the pulse-on (t_p), pulse-off (t_b) and the total cycle (t) times are found around 1.13 (± 0.08) ms, 3.39 (± 0.13) ms and 4.52 (± 0.57) ms, respectively as shown in Fig. 2c, d. As the cycle time reduces, the pulse frequency increases to 221 Hz resulting in a higher time-averaged arc power (P) of 1298 (± 5) W for the WFR of 6 m/min. A comparison of these values shows that an increase in the PTS from 5 to 7.5 mm/s at a constant WFR of 5 m/min reduces the energy input from 163 to 109 J/mm at a constant arc power of 818 (± 3) W. In contrast, the energy input increases from 109 to 173 J/mm as the WFR is increased from 5 to 6 m/min at a constant PTS of 7.5 mm/s.

3.2 Probing single-track multi-layer wall deposits

Figure 3 shows the single-track deposits and the corresponding transverse cross-sections, which are taken at the

Fig. 3 Top view and corresponding transverse cross-sections of single-track wall deposits for three conditions: **a, b** S1 (WFR: 5 m/min, PTS: 5 mm/s, E: 163 J/mm), **c, d** S2 (WFR: 5 m/min, PTS: 7.5 mm/s, E: 109 J/mm) and **e, f** S3 (WFR: 6 m/min, PTS: 7.5 mm/s, E: 173 J/mm). w , h and p are the width, height and penetration for the deposited track



mid-length of the track for the three process conditions, presented in Table 2. A comparison between Fig. 3a–d shows a decrease in the track dimensions with an increase in the PTS from 5 to 7.5 mm/s, which is attributed to a decrease in the energy input per unit length from 163 to 109 J/mm. For example, the track width (w) reduces from 8.9 (± 0.2) to 6.8 (± 0.1) mm, track height (h) from 2.2 (± 0.1) to 1.8 (± 0.1) mm and the penetration (p) from 1.4 (± 0.1) to 1.3 (± 0.1) mm as the PTS increases from 5 to 7.5 mm/s.

In contrast, Fig. 3c–f show that the track dimensions increase as the WFR is increased from 5 to 6 m/min, which is attributed to a rise in the energy input per unit length from 109 to 173 J/mm. For example, the track width (w) increases from 6.8 (± 0.1) to 9.8 (± 0.2) mm, track height (h) from 1.8 (± 0.1) to 2.4 (± 0.1) mm and the penetration (p) from 1.3 (± 0.1) to 2.4 (± 0.1) mm as the WFR is increased from 5 to 6 m/min. In summary, an increase in WFR and a decrease in PTS result in higher energy input and larger track dimensions.

The measured single-track width (w) in Fig. 3 at different WFR and PTS is used further to find out a suitable hatch spacing ($\delta = 0.63 w$) for multi-track depositions. Table 3 shows the measured values of the single-track width (w) and height (h), the estimated hatch spacing ($\delta = 0.63 w$) and the layer height for the multi-track multi-layer deposition for three different process conditions. The layer height is set as equal to the height of the deposited track for a process condition.

Figure 4a, b shows the top and front view of the single-track nine-layer deposit for 5 m/min WFR and 5 mm/s PTS. The corresponding cross-section at the mid-length of the track is shown in Fig. 4c, d. The dimensional inconsistency along the wall height, which is referred to as the surface waviness is estimated as $(w_m - w_e)/2$, where w_m is the measured widths at different heights, and w_e is the effective wall width that is achieved after machining. Figure 4d shows the deposit cross-sections with grids, which are used to measure w_m at an equal interval of 0.5 mm along the wall height and the effective wall width (w_e). Although the grids are shown up to the top layer of the deposit in Fig. 4d, the variation in the measured width (w_m) and surface waviness for each sample are measured up to the effective height of the wall (h_e), i.e. height of the inscribed rectangle only. The transverse cross-sectional profiles of single-track five-layer

and single-track nine-layer wall deposits at all three process conditions (Table 2) are shown in Fig. 11 in Appendix 1.

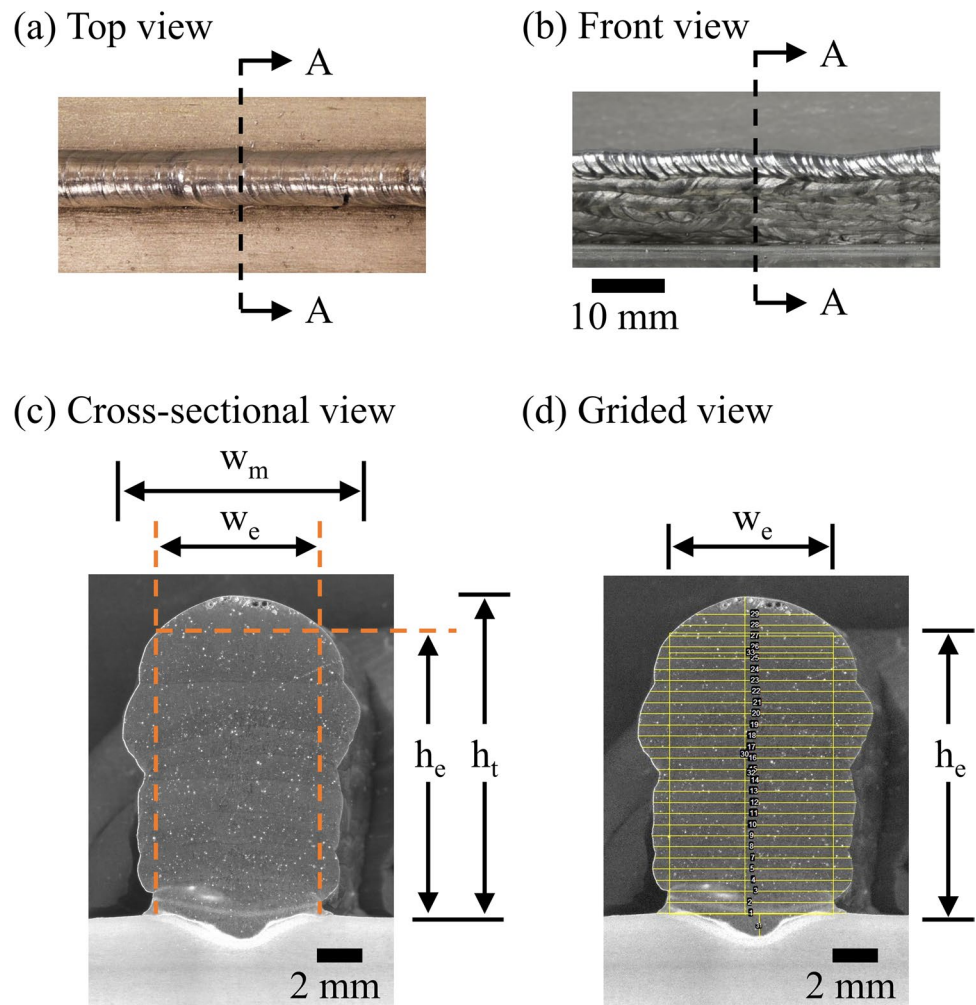
Figure 5a, b shows the measured width w_m and the surface waviness for the five-layer and nine-layer wall deposits, respectively at three process conditions (Table 2). The measured values of the wall width are smaller close to the substrate and increase slightly along the wall height. Secondly, the wall width increases with an increase in the energy input. For example, Fig. 5a shows that the average measured wall widths (w_m) for the five-layer wall deposits are 6.4 (± 0.2) mm, 8.4 (± 0.3) mm and 8.8 (± 0.2) mm for energy inputs per unit length of 109 J/mm, 163 J/mm, and 173 J/mm, respectively. For the nine-layer wall deposit, the average wall widths are 7.3 (± 0.1) mm, 8.8 (± 0.3) mm and 9.4 (± 0.2) mm for the energy inputs of 109 J/mm, 163 J/mm, 173 J/mm, respectively as shown in Fig. 5b. Thirdly, the width of the wall deposits along their corresponding heights becomes more consistent with an increase in the energy input for the range of process conditions (Table 2) considered here. The percentage variability in the measured widths (w_m) along the wall height represents the dimensional inconsistency of the walls, which are found around 7%, 4% and 3% for five-layer walls deposited at three energy inputs of 109 J/mm, 163 J/mm, 173 J/mm, respectively. The similar nature of percentage variability in measured widths is noted for the nine-layer walls (Fig. 5b) also, which decreases from 9% for the lowest energy input of 109 J/mm to 3% for the highest energy input of 173 J/mm.

The effective widths (w_e) of the five-layer wall deposits are measured after machining of the surface unevenness. The effective wall widths (w_e) are found to increase with the energy input as 5.2 (± 0.2) mm for 109 J/mm, 7.5 (± 0.4) mm for 163 J/mm and 8.7 (± 0.1) mm for 173 J/mm. The corresponding surface waviness variation through the wall height, which is estimated as $(w_m - w_e)/2$, is plotted in Fig. 5a. The average surface waviness is found to be around 0.59 (± 0.06) mm, 0.47 (± 0.07) mm and 0.26 (± 0.04) mm for the energy inputs of 109 J/mm, 163 J/mm and 173 J/mm, respectively. Likewise, the effective wall widths (w_e) of the nine-layer wall deposits also increase with energy input as 5.8 (± 0.5) mm for 109 J/mm, 7.1 (± 0.3) mm for 163 J/mm and 8.0 (± 0.2) mm for 173 J/mm. The corresponding surface waviness variation through the wall height is plotted in Fig. 5b. The average surface waviness values are around

Table 3 Hatch spacing, layer height and track dimensions for three process conditions

Set no.	WFR m/min	PTS mm/s	Energy input E , J/mm	Single-track width w , mm	Single-track height h , mm	Hatch spacing δ , mm	Layer height mm
S1	5	5	163	8.9 (± 0.2)	2.2 (± 0.1)	5.6	2.2
S2	5	7.5	109	6.8 (± 0.1)	1.8 (± 0.1)	4.3	1.8
S3	6	7.5	173	9.8 (± 0.2)	2.4 (± 0.1)	6.2	2.4

Fig. 4 **a** Top, **b** front and **c** transverse cross-sectional views of a single-track nine-layer wall deposit at 5 m/min WFR and 5 mm/s PTS and **d** cross-section with grid to measure wall width (w_m) at equal interval of 0.5 mm through the wall heights and the effective wall width (w_e). The effective and net wall height are measured as h_e and h_t , respectively



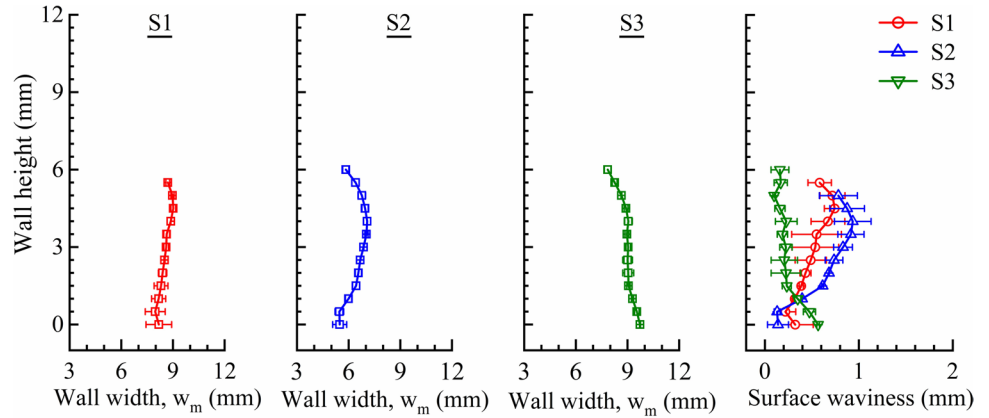
0.87 (± 0.25) mm, 0.81 (± 0.02) mm and 0.72 (± 0.03) mm. A comparison of the variations in surface waviness through the height for both five-layer and nine-layer wall deposits in Fig. 5a, b shows a tendency of increasing surface undulation with an increase in the number of layers. Pattanayak et al. [31] also reported an increase in the surface waviness as the deposition moved towards the upper layers for single-track multi-layer GTA-DED using structural steel filler wire.

An increase in the WFR and decrease in the PTS result in higher energy input per unit length and larger build height, which is attributed to a higher volume of filler wire deposition per unit track length. The effective height (h_e) of the five-layer wall deposits is found to be around 4.8 (± 1.0) mm, 5.5 (± 0.8) mm and 6.2 (± 0.5) mm corresponding to the energy inputs of 109 J/mm, 163 J/mm and 173 J/mm. Likewise, the effective height of the nine-layer wall deposits is found as 8.3 (± 0.9) mm, 9.2 (± 0.6) mm and 10.4 (± 0.3) mm for energy inputs of 109 J/mm, 163 J/mm and 173 J/mm, respectively. It is noteworthy that the increasing energy input per unit length for the aforementioned cases is either due to higher WFR or lower PTS. A similar increase in the

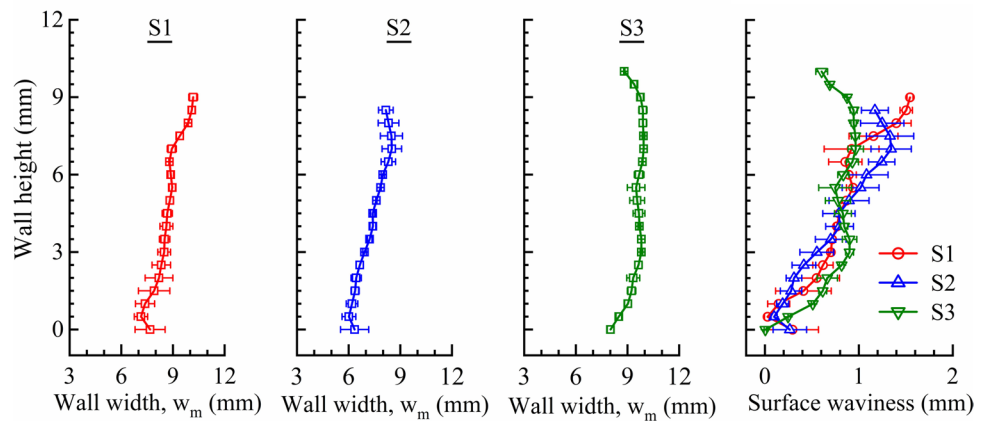
wall height with a smaller PTS and resulting higher energy input has been reported by Le et al. [18] for GMA-DED with a stainless steel filler wire.

The dimensional variations of the wall deposits indicate a need to examine the uniformity in the mechanical properties along the wall height. Figure 6 presents the variation in the measured microhardness along the centreline of the wall deposits at three different conditions (Table 2) for the single-track nine-layer deposits. The measured hardness is found to be higher closer to the substrate for all three conditions, which is a likely result of a harder structure due to the rapid heat dissipation through the substrate and a high cooling rate [32]. As the deposition moves to the upper layers, the rate of heat dissipation through the deposited layers and substrate slows down resulting in a coarser structure and slightly lower hardness as shown in Fig. 6. The average microhardness values are found to be nearly the same 51 (± 3) HV for all the three energy input conditions (Table 2). Pramod et al. [32] also reported the variation in microhardness along deposition height, which reduces from 58 HV in the initial layers to 51 HV in the middle layers, followed by

Fig. 5 Variation in measured width (w_m) and surface waviness for single-track (a) five-layer and (b) nine-layer wall deposits at three process conditions S1 (WFR: 5 m/min, PTS: 5 mm/s, E: 163 J/mm), S2 (WFR: 5 m/min, PTS: 7.5 mm/s, E: 109 J/mm) and S3 (WFR: 6 m/min, PTS: 7.5 mm/s, E: 173 J/mm)

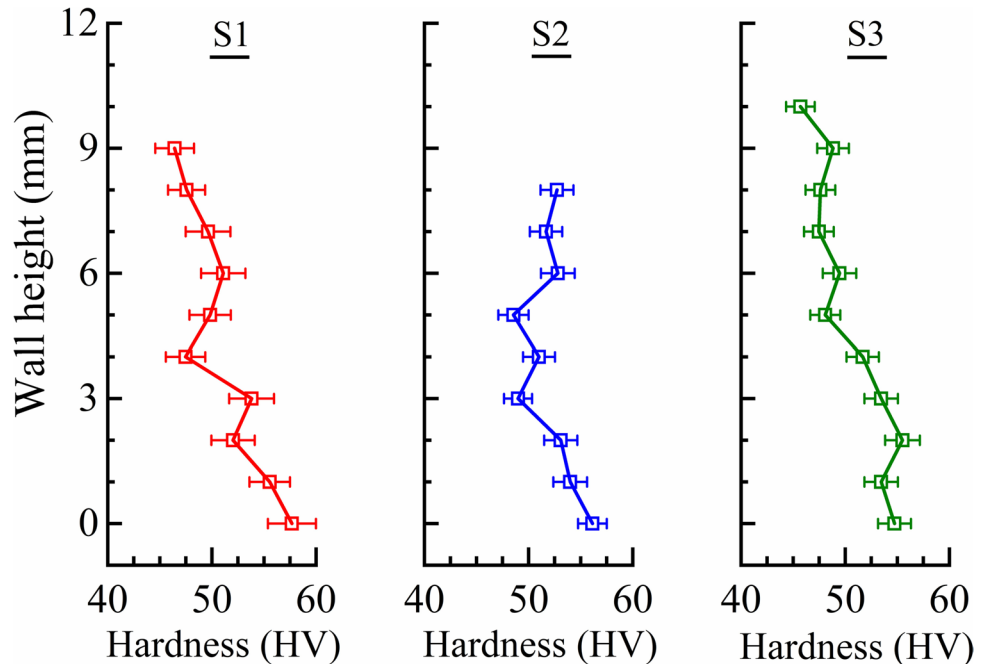


(a)



(b)

Fig. 6 Variation in the measured microhardness along wall height for single-track nine-layer deposits at three conditions (Table 2). The measuring locations are represented by the open square symbols. The process conditions are S1 (WFR: 5 m/min, PTS: 5 mm/s, E: 163 J/mm), S2 (WFR: 5 m/min, PTS: 7.5 mm/s, E: 109 J/mm) and S3 (WFR: 6 m/min, PTS: 7.5 mm/s, E: 173 J/mm)



46 HV in the top layers during the single-track multi-layer cylinder deposition using AA4043 filler wire and AA6061 substrate.

3.3 Probing multi-track multi-layer deposits

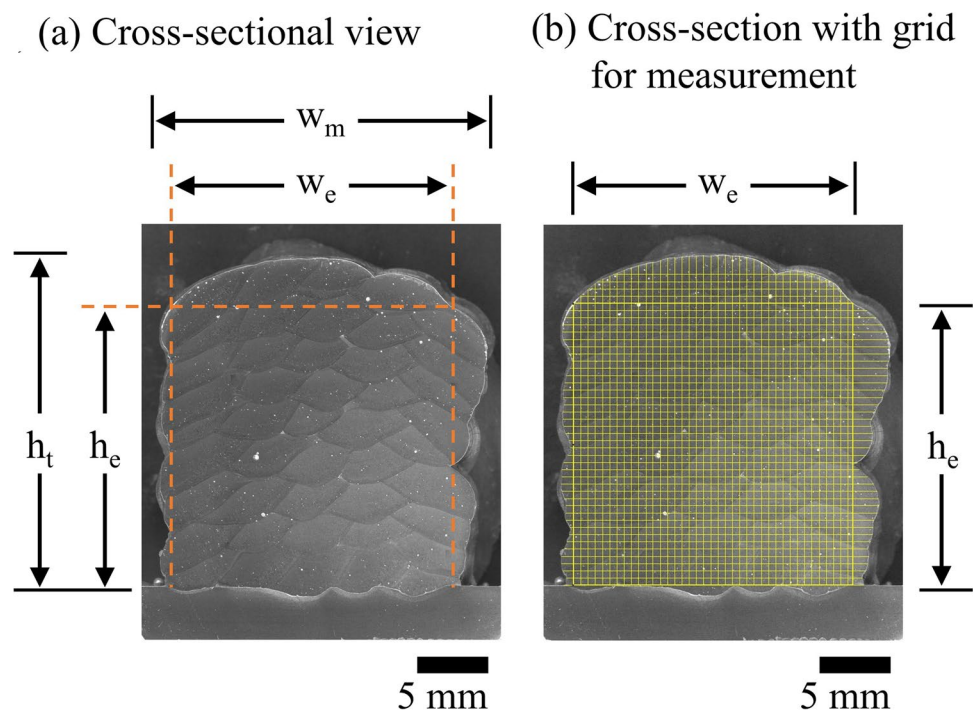
Figure 7a, b shows the transverse cross-section at the mid-length of a sample five-track nine-layer deposit at 5 m/min WFR and 7.5 mm/s PTS, which indicates the partial overlap between adjacent tracks and successive layers without any distinct lack-of-fusion (Fig. 7a). Fig. 12 in Appendix 2 shows the transverse cross-sectional profiles of five-track nine-layer build deposits at other two process conditions; S1 and S3 (Table 2). The surface waviness along the deposit height is estimated for each build using the approach mentioned in Section 3.2. In contrast, the waviness along the top surface is estimated as $(h_t - h_e)$, where h_t is the measured build height at an equal interval along the width, and h_e is the effective height after machining, shown in Fig. 7. Figure 7b shows the deposit cross-sections with grids, which are used to measure build width (w_m) and h_t at an equal interval of 0.5 mm through the build height and width, respectively, and the effective build height (h_e) and the effective build width (w_e).

Figure 8a–c shows the measured build width (w_m) along the build height for the five-track nine-layer deposits for three process conditions. The build width remains nearly the same with little variations through the build height. A comparison of Fig. 8a–c with the measured widths (w_m) in Fig. 5 shows a reduced variation in the measured width for

the multi-track multi-layer builds than that for the single-track multi-layer walls. This is attributed to the deposition of multiple adjacent overlapped tracks for the multi-track multi-layer deposits. Figure 8a–c also shows an increase in the measured build width with an increase in the energy input, which is attributed to the increase in the track width (w) as energy input increases. For example, the average values of the measured width (w_m) are around 21.0 (± 0.2) mm, 24.2 (± 0.4) mm and 32.7 (± 0.1) mm for the energy inputs of 109 J/mm, 163 J/mm and 173 J/mm, respectively. The average values of percentage variability in the measured widths are decreased from 4% for the lowest energy input of 109 J/mm to 2% for the highest energy input of 173 J/mm.

The effective width (w_e) of each deposit is measured after the surface unevenness is machined off. The average values of the measured effective width (w_e) are found to increase with energy input. The average effective widths (w_e) are around 18.0 (± 0.6) mm, 21.7 (± 0.5) mm and 30.5 (± 0.4) mm for the energy inputs of 109 J/mm, 163 J/mm and 173 J/mm, respectively. The corresponding average surface waviness values through the build height, estimated as $(w_m - w_e)/2$, are found to reduce with energy input as shown in Fig. 8d. For example, the average surface waviness values are around 1.60 (± 0.14) mm, 1.31 (± 0.28) mm and 1.07 (± 0.20) mm for the energy inputs of 109 J/mm, 163 J/mm and 173 J/mm, respectively. For multi-layer GMA-DED, using a 1.2 mm diameter aluminium alloy (ER5356) filler wire, Scotti et al. [33] have reported a relatively smaller range (0.3 to 0.8 mm) of surface waviness,

Fig. 7 **a** Transverse cross-section at mid-length of a sample five-track nine-layer deposit for S2 (WFR: 5 m/min, PTS: 7.5 mm/s) condition and **b** cross-section with grids to measure build width (w_m) variations at an equal interval of 0.5 mm through the effective build height, build height (h_t) variations at an equal interval of 0.5 mm through the effective build width, and the effective build width (w_e) and the effective build height (h_e)



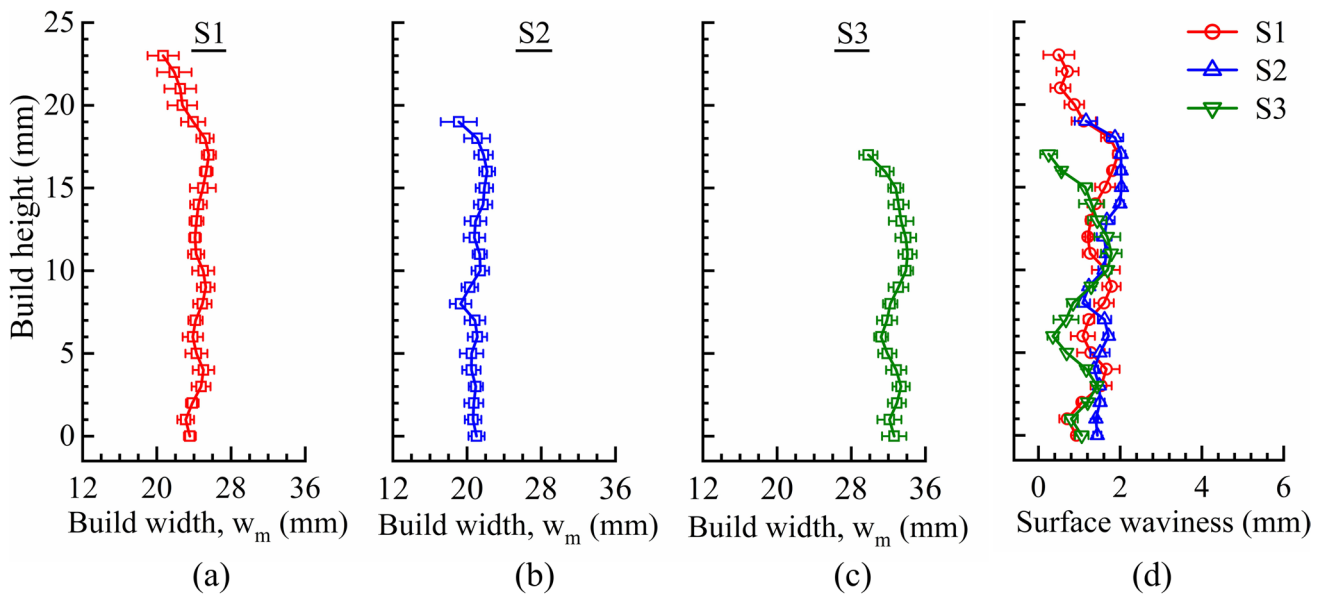


Fig. 8 Variation in **a–c** measured build width (w_m) and **d** surface waviness along effective build height for five-track nine-layer builds at three conditions: S1 (WFR: 5 m/min, PTS: 5 mm/s, E: 163 J/mm),

S2 (WFR: 5 m/min, PTS: 7.5 mm/s, E: 109 J/mm) and S3 (WFR: 6 m/min, PTS: 7.5 mm/s, E: 173 J/mm)

which is attributed to an improved control over the filler wire deposition rate.

Figure 9a–c shows the measured build height (h_t), and Fig. 9d shows the waviness along the top surface for the sample five-track nine-layer deposits at three process conditions (Table 2). The measurements are taken from the left edge to the right edge of the transverse cross-sectional

profile of each build, i.e. across the effective wall width (w_e), as shown in sample Fig. 7b. The measured values of the build height are smaller at the start of the first track, increase along the build width and become smaller again for the last (fifth) track due to the typical curved profile of the first and the last track of each layer. The average measured build height (h_t) values are found as 21.5 (± 0.2) mm, 26.3

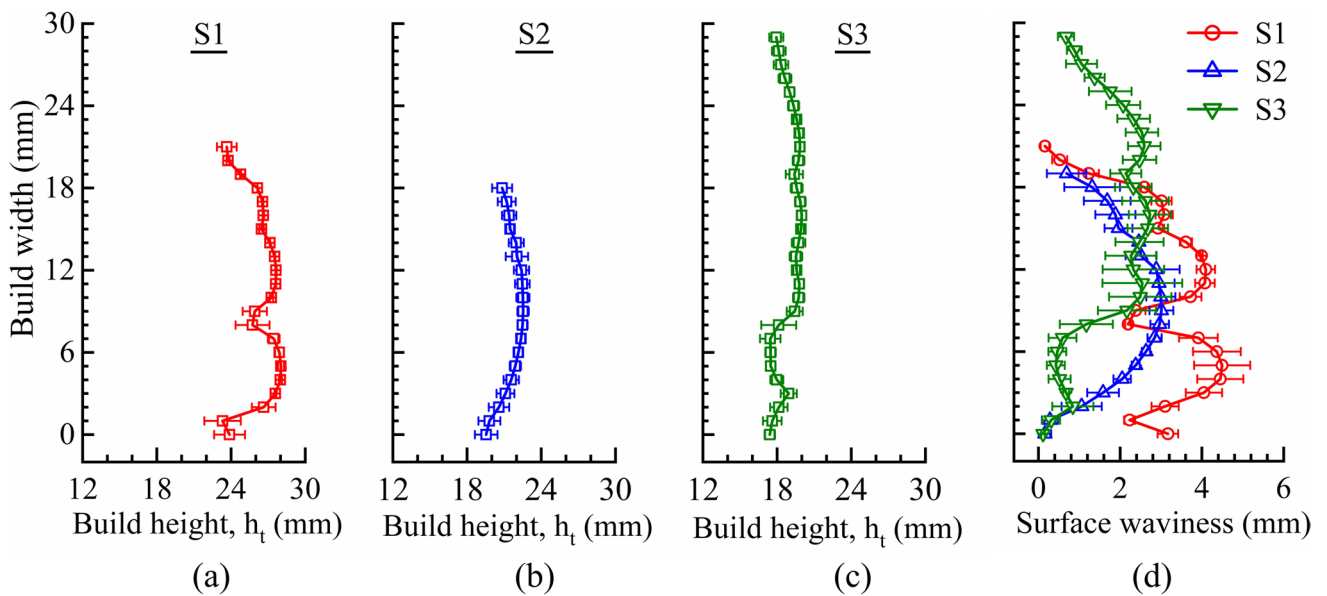


Fig. 9 Variation in **a–c** measured build height (h_t) and **d** top surface waviness along effective build width for five-track nine-layer deposits at three conditions, S1 (WFR: 5 m/min, PTS: 5 mm/s, E: 163 J/mm),

S2 (WFR: 5 m/min, PTS: 7.5 mm/s, E: 109 J/mm) and S3 (WFR: 6 m/min, PTS: 7.5 mm/s, E: 173 J/mm)

(± 0.1) mm and 18.7 (± 0.8) mm for the energy inputs of 109 J/mm, 163 J/mm and 173 J/mm, respectively. The shortest build height for the maximum energy input is attributed to excessive melting of already deposited layers and filler wire and uncontrolled flow of molten metal. Like percentage variability of width for walls (Fig. 5) and builds (Fig. 8), the percentage variability in the measured build heights (h_t) is found minimum around 3% for the maximum energy input of 173 J/mm as shown in Fig. 9.

The effective deposit height (h_e) is measured after machining of the top surface unevenness and found as 19.5 (± 0.1) mm for an energy input of 109 J/mm, 23.5 (± 0.3) mm for 163 J/mm and 17.3 (± 0.7) mm for 173 J/mm. Figure 9d shows the corresponding variation of the top surface waviness through the build width, which is estimated as ($h_t - h_e$). The average value of surface waviness through the build width is found around 3.06 (± 0.11) mm, 2.06 (± 0.21) mm and 1.78 (± 0.38) mm corresponding to the energy inputs of 163 J/mm, 109 J/mm and 173 J/mm. It is further noteworthy that the effective height of the five-track nine-layer builds is always greater than that for the single-track nine-layer walls, which is attributed to the restricted flow of the molten metal due to multiple overlapping of adjacent tracks for the multi-track builds [10]. Overall, the surface waviness along both the build height (Fig. 8d) and width (Fig. 9d) is found to be the minimum for the maximum energy input per unit length within the range of process conditions considered here.

Figure 10 presents the variation in the measured microhardness along the centreline of the five-track nine-layer builds. The measured hardness is higher near the substrate and reduces with build height. A similar variation of the

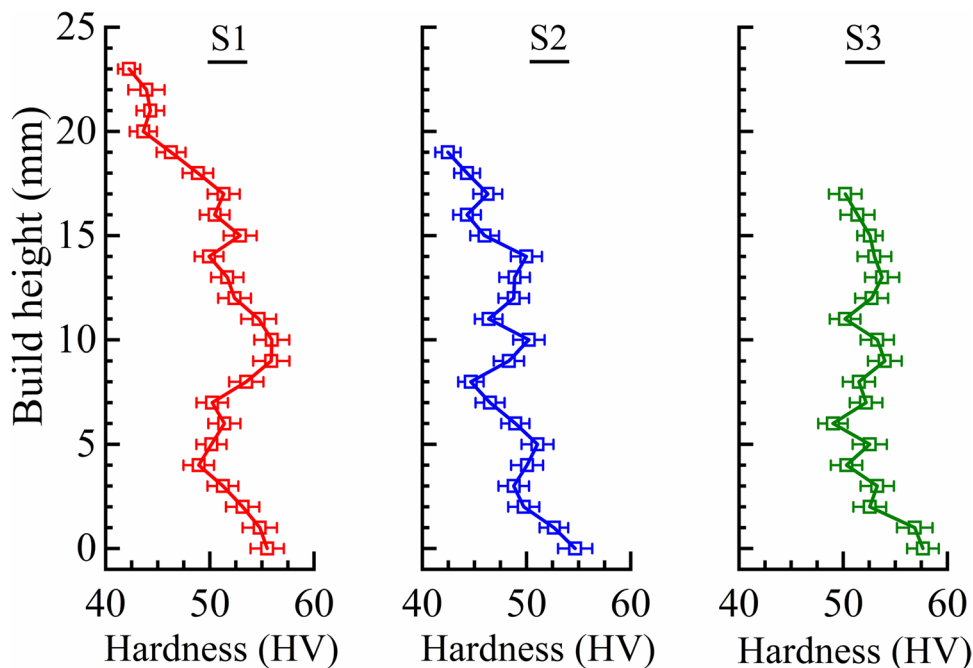
measured hardness is also noted for the single-track nine-layer walls in Fig. 6. The higher hardness in the bottom layers near the substrate can be attributed to a finer structure as a result of faster heat dissipation through the substrate and higher cooling rate, which is also reported in literature [32]. The average microhardness of the five-track nine-layer builds is found around 51 (± 4) HV, 48 (± 3) HV and 52 (± 2) HV corresponding to the energy input of 163 J/mm, 109 J/mm and 173 J/mm.

4 Summary and conclusions

An experimental GMA-DED set-up is used to examine the dimensional consistency for GMA-DED of single-track multi-layer walls and multi-track multi-layer builds using an aluminium alloy filler wire. The real-time current and voltage transients are measured to estimate the effective arc power and energy input per unit length. The effective arc power and energy input per unit length increase with an increase in WFR at a given PTS. In contrast, the energy input per unit length reduces with an increase in PTS at a constant WFR. The sensitivity of the surface waviness for the single-track and multi-track multi-layer deposits to the energy input per unit length is examined in a rigorous manner. The microhardness distributions along the build heights are also examined and reported. The following conclusions are drawn from the present experimental investigation.

- An increase in the energy input per unit length results in reduced variations in the build width and surface wavi-

Fig. 10 Variation in the measured microhardness along build height for five-track nine-layer deposits at three conditions: S1 (WFR: 5 m/min, PTS: 5 mm/s, E: 163 J/mm), S2 (WFR: 5 m/min, PTS: 7.5 mm/s, E: 109 J/mm) and S3 (WFR: 6 m/min, PTS: 7.5 mm/s, E: 173 J/mm) (Table 2). The measuring locations are shown by open square symbols



ness, which is attributed to an improved spreading of molten metal at a higher energy input.

- The measured microhardness of the multi-layer deposits is slightly higher at the bottom layers near the substrate. This can be attributed to a finer structure as a result of faster heat dissipation through the substrate and higher cooling rate although a detailed investigation is required to evaluate this further. The energy input per unit length has shown little influence on the average microhardness for the range of process conditions considered here.

Appendix 1 Single-track multi-layer wall deposits

Figure 11a–c and d–f show the transverse cross-section profiles of the single-track five- and nine-layer aluminium wall deposits at three different process conditions; S1–S3 (Table 2). As the energy input increases, the average width of the wall is found to increase for five- and nine-layer wall

deposits. This is attributed to the increase in the rate of depositing material with an increase in the WFR at constant PTS or a decrease in the PTS at constant WFR. The measured width (w_m) and surface waviness along the wall height are presented in Fig. 5a, b for the single-track five- and nine-layer wall deposits shown in Figs 11a–f, followed by a detailed discussion in Section 3.2.

Appendix 2 Multi-track multi-layer build deposits

Figure 12a, b shows the transverse cross-section profiles of the five-track nine-layer aluminium builds at two different process conditions; S1 and S3 (Table 2). As observed in Fig. 11a–c and d–f, the overall build width is found to increase with an increase in the energy input for the five-track nine-layer build deposits shown in Fig. 12a, b. The measured build width (w_m) and surface waviness along the build height are presented in Fig. 8a–d for the five-track

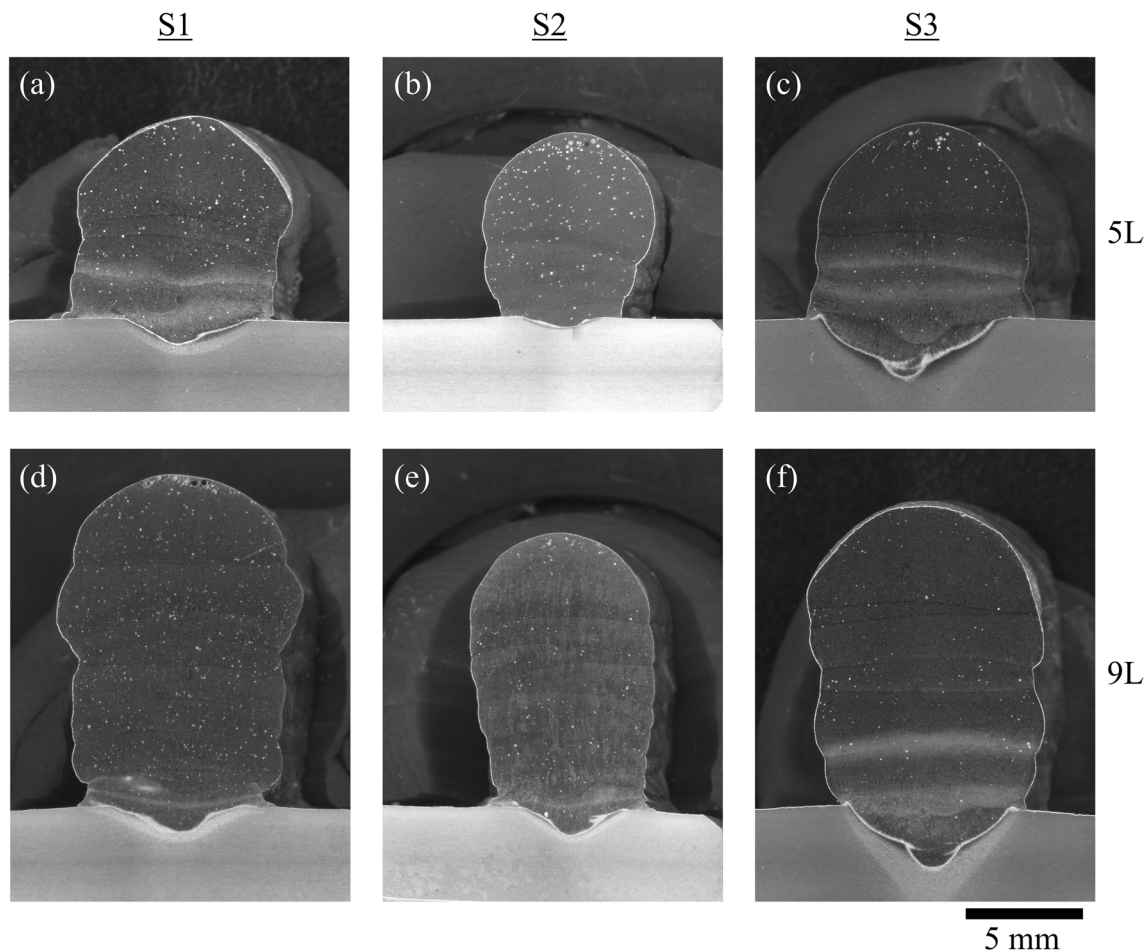


Fig. 11 Transverse cross-sectional views of the single-track **a–c** five-layer and **d–f** nine-layer wall deposits at three process conditions S1 (WFR: 5 m/min, PTS: 5 mm/s, E: 163 J/mm), S2 (WFR: 5 m/min, PTS: 7.5 mm/s, E: 109 J/mm) and S3 (WFR: 6 m/min, PTS: 7.5 mm/s, E: 173 J/mm)

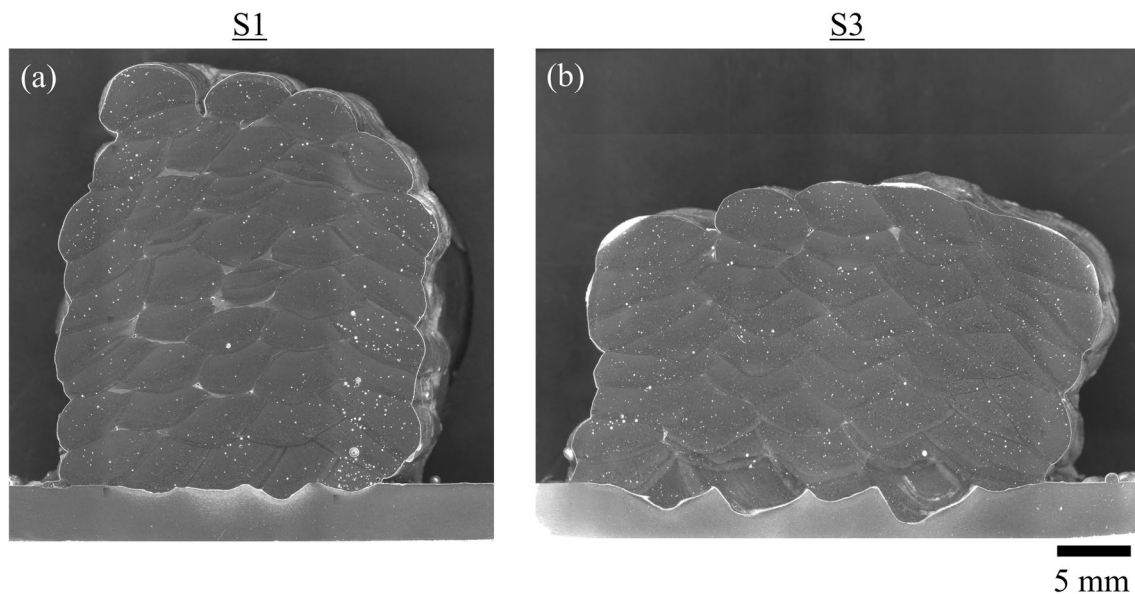


Fig. 12 Transverse cross-sectional views of the five-track nine-layer build deposits at two different conditions; **a** S1 (WFR: 5 m/min, PTS: 5 mm/s, E: 163 J/mm) and **b** S3 (WFR: 6 m/min, PTS: 7.5 mm/s, E:

173 J/mm). The transverse cross-sectional profile at S2 condition is already shown in Fig. 4

nine-layer wall deposits at all three process conditions (Table 2), followed by a detailed discussion in Section 3.2. Further, the surface waviness along the top surface across the effective build width is also presented in Fig. 9d for all three process conditions (Table 2) and discussed subsequently.

Acknowledgements We gratefully acknowledge the support from the Indo-German Science and Technology Centre (IGSTC) grant IGSTC/Call 2020/RAMFLICS/52/2021-22/253 for carrying out this work at the Indian Institute of Technology Bombay.

Author contribution PKC: experimentation, analysis, measurements, writing—original draft. BKB: experimentation, analysis, measurements, writing—review and editing. AD: analysis, measurements, writing—review and editing. SFG: conceptualization, writing—review and editing. AD: conceptualization, writing—review and editing.

Declarations

Competing interests The authors declare no competing interests.

References

- Lockett H, Ding J, Williams S, Martina F (2017) Design for wire + arc additive manufacture: design rules and build orientation selection. *J Eng Des* 28:568–598. <https://doi.org/10.1080/09544828.2017.1365826>
- DebRoy T, Wei HL, Zuback JS, Mukherjee T, Elmer JW, Milewski JO et al (2018) Additive manufacturing of metallic components – process, structure and properties. *Prog Mater Sci* 92:112–224. <https://doi.org/10.1016/j.pmatsci.2017.10.001>
- Wu B, Pan Z, Ding D, Cuiuri D, Li H, Xu J et al (2018) A review of the wire arc additive manufacturing of metals: properties, defects and quality improvement. *J Manuf Processes* 35:127–139. <https://doi.org/10.1016/j.jmapro.2018.08.001>
- Chaurasia PK, Goecke SF, De A (2022) Real-time monitoring of temperature field, metal transfer and cooling rate during gas metal arc-directed energy deposition. *Sci Technol Weld Join* 27:512–521. <https://doi.org/10.1080/13621718.2022.2080447>
- Williams SW, Martina F, Addison AC, Ding J, Pardal G, Colegrove P (2016) wire + arc additive manufacturing. *Mater Sci Technol* 32:641–647. <https://doi.org/10.1179/1743284715Y.0000000073>
- Wang Y, Zhang C, Lu J, Bai L, Zhao Z, Han J (2020) Weld reinforcement analysis based on long-term prediction of molten pool image in additive manufacturing. *IEEE Access* 8:69908–69918. <https://doi.org/10.1109/access.2020.2986130>
- Li Y, Polden J, Pan Z, Cui J, Xia C, He F et al (2022) A defect detection system for wire arc additive manufacturing using incremental learning. *J Ind Inf Integr* 27:100291. <https://doi.org/10.1016/j.jii.2021.100291>
- Hauser T, Reisch RT, Seebauer S, Parasar A, Kamps T, Casati R et al (2021) Multi-material wire arc additive manufacturing of low and high alloyed aluminium alloys with in-situ material analysis. *J Manuf Processes* 69:378–390. <https://doi.org/10.1016/j.jmapro.2021.08.005>
- Li Y, Han Q, Zhang G, Horváth I (2018) A layers-overlapping strategy for robotic wire and arc additive manufacturing of multi-layer multi-bead components with homogeneous layers. *J Adv Manuf Technol* 96:3331–3344. <https://doi.org/10.1007/s00170-018-1786-3>
- Chaurasia PK, Goecke S-F, De A (2023) Monitoring melt pool asymmetry in gas metal arc-directed energy deposition. *Sci Technol Weld Join* 1-9. <https://doi.org/10.1080/13621718.2023.2168933>
- Ali Y, Henckell P, Hildebrand J, Reimann J, Bergmann JP, Barnikol-Oettler S (2019) Wire arc additive manufacturing of hot work tool steel with CMT process. *J Mater Process Technol* 269:109–116. <https://doi.org/10.1016/j.jmatprotec.2019.01.034>

12. Rodrigues TA, Duarte V, Avila JA, Santos TG, Miranda RM, Oliveira JP (2019) Wire and arc additive manufacturing of HSLA steel: effect of thermal cycles on microstructure and mechanical properties. *Addit Manuf* 27:440–450. <https://doi.org/10.1016/j.addma.2019.03.029>
13. Ogino Y, Asai S, Hirata Y (2018) Numerical simulation of WAAM process by a GMAW weld pool model. *Weld World* 62:393–401. <https://doi.org/10.1007/s40194-018-0556-z>
14. Le VT, Mai DS, Hoang QH (2020) A study on wire and arc additive manufacturing of low-carbon steel components: process stability, microstructural and mechanical properties. *J Braz Soc Mech Sci Eng* 42:480. <https://doi.org/10.1007/s40430-020-02567-0>
15. Xia C, Pan Z, Polden J, Li H, Xu Y, Chen S et al (2020) A review on wire arc additive manufacturing: monitoring, control and a framework of automated system. *J Manuf Syst* 57:31–45. <https://doi.org/10.1016/j.jmsy.2020.08.008>
16. Wu B, Pan Z, Chen G, Ding D, Yuan L, Cuiuri D et al (2019) Mitigation of thermal distortion in wire arc additively manufactured Ti6Al4V part using active interpass cooling. *Sci Technol Weld Join* 24:484–494. <https://doi.org/10.1080/13621718.2019.1580439>
17. Zhai W, Wu N, Zhou W (2022) Effect of interpass temperature on wire arc additive manufacturing using high-strength metal-cored wire. *Met* 12:212. <https://doi.org/10.3390/met12020212>
18. Le VT, Mai DS, Bui MC, Wasmer K, Nguyen VA, Dinh DM et al (2022) Influences of the process parameter and thermal cycles on the quality of 308L stainless steel walls produced by additive manufacturing utilizing an arc welding source. *Weld World* 66:1565–1580. <https://doi.org/10.1007/s40194-022-01330-4>
19. Novelino ALB, Carvalho GC, Ziberov M (2022) Influence of WAAM-CMT deposition parameters on wall geometry. *Adv Ind Manuf Eng* 5:100105. <https://doi.org/10.1016/j.aime.2022.100105>
20. Chaurasia PK, Goecke SF, De A (2023) Towards real-time monitoring of metal transfer and melt pool temperature field in gas metal arc directed energy deposition. *Weld World* 1-11. <https://doi.org/10.1007/s40194-023-01534-2>
21. Geng H, Li J, Xiong J, Lin X, Huang D, Zhang F (2018) Formation and improvement of surface waviness for additive manufacturing 5A06 aluminium alloy component with GTAW system. *Rapid Prototyp J* 24:342–350. <https://doi.org/10.1108/rpj-04-2016-0064>
22. Zhou X, Zhang H, Wang G, Bai X (2016) Three-dimensional numerical simulation of arc and metal transport in arc welding based additive manufacturing. *Int J Heat Mass Transfer* 103:521–537. <https://doi.org/10.1016/j.ijheatmasstransfer.2016.06.084>
23. Ou W, Knapp GL, Mukherjee T, Wei Y, DebRoy T (2021) An improved heat transfer and fluid flow model of wire-arc additive manufacturing. *Int J Heat Mass Transfer* 167:120835–120835. <https://doi.org/10.1016/j.ijheatmasstransfer.2020.120835>
24. Cao H, Huang R, Yi H, Liu M, Jia L (2022) Asymmetric molten pool morphology in wire-arc directed energy deposition: evolution mechanism and suppression strategy. *Addit Manuf* 59A:103113. <https://doi.org/10.1016/j.addma.2022.103113>
25. Ge J, Ma T, Chen Y, Jin T, Fu H, Xiao R et al (2019) Wire-arc additive manufacturing H13 part: 3D pore distribution, microstructural evolution, and mechanical performances. *J Alloys Compd* 783:145–155. <https://doi.org/10.1016/j.jallcom.2018.12.274>
26. Zhou X, Tian Q, Du Y, Zhang Y, Bai X, Zhang Y et al (2021) Investigation of the effect of torch tilt and external magnetic field on arc during overlapping deposition of wire arc additive manufacturing. *Rapid Prototyp J* 27:24–36. <https://doi.org/10.1108/RPJ-03-2020-0047>
27. Xiong J, Zhang G, Gao H, Wu L (2013) Modeling of bead section profile and overlapping beads with experimental validation for robotic GMAW-based rapid manufacturing. *Rob Comput Integr Manuf* 29:417–423. <https://doi.org/10.1016/j.rcim.2012.09.011>
28. Plangger J, Schabhüttl P, Vuherer T, Enzinger N (2019) CMT additive manufacturing of a high strength steel alloy for application in crane construction. *Met* 9:650. <https://doi.org/10.3390/met9060650>
29. Ding D, Pan Z, Cuiuri D, Li H (2015) A multi-bead overlapping model for robotic wire and arc additive manufacturing (WAAM). *Rob Comput Integr Manuf* 31:101–110. <https://doi.org/10.1016/j.rcim.2014.08.008>
30. Suryakumar S, Karunakaran KP, Bernard A, Chandrasekhar U, Raghavender N, Sharma D (2011) Weld bead modeling and process optimization in hybrid layered manufacturing. *Comput-Aided Des* 43:331–344. <https://doi.org/10.1016/j.cad.2011.01.006>
31. Pattanayak S, Sahoo SK (2023) Effect of travel speed and number of layers on surface waviness of ER70S6 deposits fabricated through non-transferred wire arc additive manufacturing. *J Adhes Sci Technol*. <https://doi.org/10.1080/01694243.2023.2217541>
32. Pramod M, Kumar SM, Girinath B, Kannan AR, Kumar NP, Shanmugam NS (2020) Fabrication, characterisation, and finite element analysis of cold metal transfer-based wire and arc additive-manufactured aluminium alloy 4043 cylinder. *Weld World* 64:1905–1919. <https://doi.org/10.1007/s40194-020-00970-8>
33. Scotti FM, Teixeira FR, Silva LJ, de Araújo DB, Reis RP, Scotti A (2020) Thermal management in WAAM through the CMT Advanced process and an active cooling technique. *J Manuf Processes* 57:23–35. <https://doi.org/10.1016/j.jmapro.2020.06.007>

Publisher's note Springer Nature remains neutral with regard to jurisdictional claims in published maps and institutional affiliations.

Springer Nature or its licensor (e.g. a society or other partner) holds exclusive rights to this article under a publishing agreement with the author(s) or other rightsholder(s); author self-archiving of the accepted manuscript version of this article is solely governed by the terms of such publishing agreement and applicable law.